

The Pennsylvania State University  
**Applied Research Lab**  
P. O. Box 30  
State College, PA 16804

**Intensity Processing of DIFAR Signals**

by

G. C. Lauchle  
Nathan K. Naluai  
Thomas B. Gabrielson

Technical Report No. TR 05-010  
30 September 2005

Support by:  
Office of Naval Research, Code 321MS

Approved for Public Release, distribution unlimited

**Copy No. 11**

The Pennsylvania State University  
APPLIED RESEARCH LABORATORY  
P.O. Box 30  
State College, PA 16804

## **Intensity Processing of DIFAR Signals**

### **Final Report**

by

Gerald C. Lauchle  
Nathan K. Naluai  
Thomas B. Gabrielson

ARL Penn State Technical Report 05-010  
30 September 2005

Supported by:  
Office of Naval Research, Code 321MS

Approved for Public Release, distribution unlimited

REPORT DOCUMENTATION PAGE				Form Approved OMB No. 0704-0188	
<p>The public reporting burden for this collection of information is estimated to average 1 hour per response, including the time for reviewing instructions, searching existing data sources, gathering and maintaining the data needed, and completing and reviewing the collection of information. Send comments regarding this burden estimate or any other aspect of this collection of information, including suggestions for reducing the burden, to Department of Defense, Washington Headquarters Services, Directorate for Information Operations and Reports (0704-0188), 1215 Jefferson Davis Highway, Suite 1204, Arlington, VA 22202-4302. Respondents should be aware that notwithstanding any other provision of law, no person shall be subject to any penalty for failing to comply with a collection of information if it does not display a currently valid OMB control number.</p> <p><b>PLEASE DO NOT RETURN YOUR FORM TO THE ABOVE ADDRESS.</b></p>					
1. REPORT DATE (DD-MM-YYYY) 30 September 2005		2. REPORT TYPE Technical Report		3. DATES COVERED (From - To) 3 Feb 2003 to 30 June 2006	
4. TITLE AND SUBTITLE  Intensity Processing of DIFAR Signals				5a. CONTRACT NUMBER	
				5b. GRANT NUMBER N00014-00-G-0058	
				5c. PROGRAM ELEMENT NUMBER	
6. AUTHOR(S)  Gerald C. Lauchle, Nathan K. Naluai, Thomas B. Gabrielson				5d. PROJECT NUMBER	
				5e. TASK NUMBER	
				5f. WORK UNIT NUMBER	
7. PERFORMING ORGANIZATION NAME(S) AND ADDRESS(ES) Applied Research Laboratory, The Pennsylvania State University P. O. Box 30 State College, PA 16804-0030				8. PERFORMING ORGANIZATION REPORT NUMBER TR #05-010	
9. SPONSORING/MONITORING AGENCY NAME(S) AND ADDRESS(ES) Office of Naval Research 875 North Randolph Street Code 321MS Arlington, VA 22203				10. SPONSOR/MONITOR'S ACRONYM(S) N/A	
				11. SPONSOR/MONITOR'S REPORT NUMBER(S) N/A	
12. DISTRIBUTION/AVAILABILITY STATEMENT Approved for public release, distribution unlimited					
13. SUPPLEMENTARY NOTES N/A					
14. ABSTRACT The use of Directional Frequency Analysis of Recording (DIFAR) acoustic subsystems as underwater acoustic intensity sensors in various Navy applications is the subject of this report. Specifically, acoustic intensity processing of DIFAR signals is used to enhance the detection of submerged bodies in the forward-scattered occlusion zone. In this zone, the incident and scattered pressure components arrive at the receiver at essentially the same time. The received signal is thus completely dominated by the incident blast from the source which renders the object undetectable. The problem of scattered wave detection in the forward-direction has been a fundamental unsolved problem of acoustics, electromagnetics and optics. The experimental results presented in this report for submerged-body acoustic scattering provide some very encouraging indications that acoustic vector intensity sensors, and the associated intensity processing, is a potential solution to this problem.					
15. SUBJECT TERMS N/A					
16. SECURITY CLASSIFICATION OF:			17. LIMITATION OF ABSTRACT  None	18. NUMBER OF PAGES  38	19a. NAME OF RESPONSIBLE PERSON Gerald C. Lauchle
a. REPORT Unclassified	b. ABSTRACT Unclassified	c. THIS PAGE Unclassified			19b. TELEPHONE NUMBER (Include area code) (814) 863-7145



## ABSTRACT

The use of Directional Frequency Analysis and Recording (DIFAR) acoustic subsystems as underwater acoustic intensity sensors in various Navy applications is the subject of this report. Specifically, acoustic intensity processing of DIFAR signals is used to enhance the detection of submerged bodies in the forward-scattered occlusion zone. In this zone, the incident and scattered pressure components arrive at the receiver at essentially the same time. The received signal is thus completely dominated by the incident blast from the source which renders the object undetectable. The problem of scattered wave detection in the forward-direction has been a fundamental unsolved problem of acoustics, electromagnetics, and optics. The experimental results presented in this report for submerged-body acoustic scattering provide some very encouraging indications that acoustic vector intensity sensors, and the associated intensity processing, is a potential solution to this problem.

Deep water experiments were conducted at Lake Seneca, NY and Lake Pend Oreille, ID. Relative to the acoustic wavelengths used in the experiments, large bodies of revolution were located on the line-of-sight between a source and SSQ-53D DIFAR sonobuoys that were used as acoustic vector intensity sensors. In the Lake Pend Oreille tests, the receivers were located from 5 to 30 body lengths away from the scattering body. The source was located in the farfield of the scattering body, assuring that the incident waves were planar. The source was driven by continuous broadband random noise; thus, all of the effects of lake reverberation are included in the presented results. The basic conclusion from this work is that the phase of the acoustic intensity component formed between the pressure sensor channel and the directional channel that is orthogonal to the direction of incident wave propagation is a repeatable and strong indicator of the presence of the scattering body in the forward-scattered direction.

## ACKNOWLEDGMENTS

This work was supported by the Office of Naval Research, Code 321MS (Dr. James McEachern and Mr. Michael Wardlaw) under Contract number N00014-00-G-0058, DO-0058. We are very grateful for this support. The assistance and support provided by the Naval Air Warfare Center, Aircraft Division, Patuxent River, MD in the field tests at Lake Seneca and Lake Pend Oreille was crucial to the success of this project. In particular, our sincere thanks are given to John Joseph and his Group: Frank Mitchell, Jason Ho, and Jason Payne. The effort given by the Lake Pend Oreille experimental support team, under the direction of Steve Finley, Naval Surface Warfare Center, Acoustics Research Detachment, Bayview, ID is also sincerely appreciated. And finally, but by no means least appreciated, are the discussions, and help provided by Dr. Christopher Barber of ARL Penn State and Mr. Michael Higgins of RDA, Inc., Doylestown, PA.

## TABLE OF CONTENTS

<b>ABSTRACT</b>	ii
<b>ACKNOWLEDGEMENTS</b>	ii
<b>TABLE OF CONTENTS</b>	iii
<b>LIST OF FIGURES</b>	iv
<b>I INTRODUCTION</b>	1
<b>II ACOUSTIC INTENSITY PROCESSING</b>	2
<b>A. Fundamental Equations for Acoustic Intensity</b>	2
<b>B. Application of Intensity Processing to DIFAR Signals</b>	3
<b>C. Application of Intensity Processing to Forward Scattering</b>	4
<b>III EXPERIMENTAL STUDIES OF FORWARD SCATTERING</b>	6
<b>A. Seneca Lake Test Program</b>	7
<b>B. Lake Pend Oreille Test Program</b>	11
1. <i>Descending Target Test</i>	13
2. <i>Source Sweep Test</i>	22
3. <i>Histogram Representation</i>	28
<b>IV CONCLUSIONS</b>	28
<b>REFERENCES</b>	30

## LIST OF FIGURES

Figure 1. Beam pattern of the scattered pressure (left) and total (incident plus scattered) pressure (right) for a 10:1 fineness ratio, rigid prolate spheroid insonified by a plane wave at  $60^\circ$  incidence.<sup>10-12</sup> The incident field masks the scattered pressure. The reduced frequency for these computations is  $kd/2 = 33.3$ , where the acoustic wavenumber is  $k$  and the interfocal distance of the spheroid is  $d$ .

Figure 2. Computed phase field for the intensity component that is transverse to the incident plane wave propagation vector which insonifies a 10:1 fineness ratio, rigid prolate spheroid at  $60^\circ$  to the major axis.<sup>12-13</sup> The major axis of the spheroid is oriented vertically, and the incident wave originates in quadrant 1. The reduced frequency is  $kd/2 = 40$ .

Figure 3. Photograph of the directional sensor of a SSQ-53D DIFAR sonobuoy. The unit is negatively buoyant and is suspended by its signal cable exiting the top-side of the case.

Figure 4. Photograph of the surface float from which the DIFAR sensor is suspended at a prescribed depth. It also contains the multiplexer, FM transmitter, and batteries.

Figure 5. Diagram of the Seneca Lake Systems Measurement Platform, and the relative positions of the source, receiver, and target used in the forward scattering tests.

Figure 6. Photograph of the Seneca Lake scattering body (target).

Figure 7. Variation of the acoustic pressure during the traverse of the sensor through the line of sight which is at a depth of 62.2 m.

Figure 8. Variation of the E-W component and the N-S component of the intensity phase during the traverse of the sensor through the line of sight which is at a depth of 62.2 m.

Figure 9. Photograph of the target used in the forward-scattering experiments at Lake Pend Oreille.

Figure 10. The ITC 4141 spherical source used in the Lake Pend Oreille scattering test.

Figure 11. Schematic diagram of the scattering experiment performed at Lake Pend Oreille. The source and line array of receivers are at a depth of 123 m.

Figure 12. Details of the top-side spar buoy that supports the intensity sensor at depth, while containing the D-cell battery power pack, multiplexer, and FM radio transmitter.

Figure 13. Photograph of the deployed array of surface floats, each supporting an individual DIFAR sensor at 123 m depth.



Figure 14. Auto-spectra of the sensor *A* omni-channel voltage measured as the target was lowered through the line-of-sight at 400 ft (123 m).

Figure 15. Auto-spectra of the sensor *B* omni-channel voltage measured as the target was lowered through the line-of-sight at 400 ft (123 m).

Figure 16. Auto-spectra of the sensor *C* omni-channel voltage measured as the target was lowered through the line-of-sight at 400 ft (123 m).

Figure 17. Auto-spectra of the sensor *D* omni-channel voltage measured as the target was lowered through the line-of-sight at 400 ft (123 m).

Figure 18. Cross-spectral phase spectra measured between the omni-channel and the N-S directional channel for sensor *A* as the target drops through the line-of-sight at 400 ft (123 m).

Figure 19. Cross-spectral phase spectra measured between the omni-channel and the N-S directional channel for sensor *B* as the target drops through the line-of-sight at 400 ft (123 m).

Figure 20. Cross-spectral phase spectra measured between the omni-channel and the N-S directional channel for sensor *C* as the target drops through the line-of-sight at 400 ft (123 m).

Figure 21. Cross-spectral phase spectra measured between the omni-channel and the N-S directional channel for sensor *D* as the target drops through the line-of-sight at 400 ft (123 m).

Figure 22. Cross-spectral phase spectra measured between the omni-channel and the E-W directional channel for sensor *A* as the target drops through the line-of-sight at 400 ft (123 m).

Figure 23. Cross-spectral phase spectra measured between the omni-channel and the E-W directional channel for sensor *B* as the target drops through the line-of-sight at 400 ft (123 m).

Figure 24. Cross-spectral phase spectra measured between the omni-channel and the E-W directional channel for sensor *C* as the target drops through the line-of-sight at 400 ft (123 m).

Figure 25. Cross-spectral phase spectra measured between the omni-channel and the E-W directional channel for sensor *D* as the target drops through the line-of-sight at 400 ft (123 m).

Figure 26. Shown here are the lines-of-forward scatter due to the sweeping of the source along the ISMS barge in the E-W direction (not drawn to scale).

Figure 27. Auto-spectra of the sensor *B* omni-channel voltage measured as the forward-scatter bearing angle changes due to lateral movement of the source.

Figure 28. Auto-spectra of the sensor *C* omni-channel voltage measured as the forward-scatter bearing angle changes due to lateral movement of the source.

Figure 29. Auto-spectra of the sensor *D* omni-channel voltage measured as the forward-scatter bearing angle changes due to lateral movement of the source.

Figure 30. Cross-spectral phase spectra measured between the omni-channel and the N-S directional channel for sensor *B* as the source sweeps out the forward-scattering angles indicated on one of the abscissas. The sensor is along the  $0^\circ$  bearing.

Figure 31. Cross-spectral phase spectra measured between the omni-channel and the N-S directional channel for sensor *C* as the source sweeps out the forward-scattering angles indicated on one of the abscissas. The sensor is along the  $0^\circ$  bearing.

Figure 32. Cross-spectral phase spectra measured between the omni-channel and the N-S directional channel for sensor *D* as the source sweeps out the forward-scattering angles indicated on one of the abscissas. The sensor is along the  $0^\circ$  bearing.

Figure 33. Cross-spectral phase spectra measured between the omni-channel and the E-W directional channel for sensor *B* as the source sweeps out the forward-scattering angles indicated on one of the abscissas. The sensor is along the  $0^\circ$  bearing.

Figure 34. Cross-spectral phase spectra measured between the omni-channel and the E-W directional channel for sensor *C* as the source sweeps out the forward-scattering angles indicated on one of the abscissas. The sensor is along the  $0^\circ$  bearing. Note side-lobes at  $\pm 4.5^\circ$  as predicted by theory.

Figure 35. Cross-spectral phase spectra measured between the omni-channel and the E-W directional channel for sensor *D* as the source sweeps out the forward-scattering angles indicated on one of the abscissas. The sensor is along the  $0^\circ$  bearing. Note side-lobe presence at  $-4.5^\circ$ . The phase shifts at about  $-11^\circ$  are due to contaminating source (motorized wench engine).

Figure 36. Typical histograms from the source sweep test – sensor *C* at  $h = 61.1$ . The histogram on the left (blue) is for the target well removed from the line-of-sight, while the histogram on the right (red) is obtained for the target on the line-of-sight.

Figure 37. Typical histograms from the source sweep test – sensor *D* at  $h = 76.4$ . The histogram on the left (blue) is for the target well removed from the line-of-sight, while the histogram on the right (red) is obtained for the target on the line-of-sight.



## INTRODUCTION

In bi-static sonar, a short pulse of acoustic energy is transmitted from a source, it propagates through the medium, it scatters from a target, and the time-delayed direct and scattered signals are received by remotely positioned receivers. For most receiver, source, and target positions, the scattered signal is distinguished from the direct path signal because it arrives at a later time. This time delay, however, becomes essentially zero when the target is on the line-of-sight between the receiver and source. The incident and scattered pressure components arrive at the receiver at the same time and the received signal is dominated by the incident blast from the source. The problem of detecting the target in this forward-scattered occlusion zone is considered unsolved at present. The significance of the problem at high frequencies has been discussed by many investigators<sup>1-8</sup> due to its application in imaging, radar, and sonar systems. For example, when light is obstructed by a circular disk, it is in the forward-scattered region where the Poisson spot can be observed and the classic Airy diffraction pattern is created. In atmospheric optics, forward scattering from small water droplets causes the colored rings around the moon (lunar corona). It is also the forward scatter from a sphere in the high frequency limit that gives rise to the extinction paradox in which the total scattering cross section of a sphere is twice the geometrical cross section of the sphere.<sup>9</sup> Previous investigations into the forward-scattering of waves by objects emphasize calculations – or measurements – of the scalar field magnitude. In acoustics, this amounts to computing or measuring the acoustic pressure field in the far-field region of the scattering body.

The occlusion zone problem can also be addressed using acoustic intensity processing of the signals received by acoustic vector intensity sensors.<sup>10-13</sup> Acoustic intensity is the *product* of acoustic pressure and acoustic particle velocity at the same point in space. In these earlier studies, we consider as a generic scattering object a rigid prolate spheroid insonified by monochromatic plane waves at arbitrary angles of incidence. It was shown that the pressure gradients created within interference regions of the total (incident plus scattered) field cause significant variations in both the reactive intensity and the phase angle between pressure and particle velocity. The forward-scattered occlusion zone is composed of a mixture of incident and scattered wave components; therefore, it is a region rich in acoustic pressure gradients and intensity phase variations.

Now the SSQ-53D series DIFAR sonobuoy is equipped with an omni-directional scalar pressure transducer, and a pair of collocated directional sensors that provide signals proportional to two orthogonal components of acoustic particle velocity. It is a straightforward procedure to process these three signals to yield two components of acoustic intensity. The present paper describes experiments that serve two purposes: 1) demonstrate that DIFAR sensors can be used to measure underwater acoustic vector intensity, and 2) use DIFAR sensors in an intensity-based demonstration of target detection in the forward- scattered occlusion zone. Independent experiments conducted at Seneca Lake in upstate New York, and at Lake Pend Oreille in northern Idaho are described.

## II ACOUSTIC INTENSITY PROCESSING

In this section we outline the basic equations of acoustic intensity, how intensity processing may be performed on the signals received by a standard DIFAR sensor, and how intensity processing might help solve the forward-scattered occlusion zone problem.

### A. Fundamental Equations for Acoustic Intensity

The instantaneous acoustic intensity at a point  $\vec{r}$  in space is defined as the product of acoustic pressure and particle velocity:

$$\vec{I}_i = p(\vec{r}, t) \vec{u}(\vec{r}, t). \quad (1)$$

When complex notation is used to describe a generic harmonic acoustic wave of frequency  $\omega$ , a spatial phase term  $\varphi(\vec{r})$  is used to indicate the phase between pressure and particle velocity. The instantaneous acoustic intensity can then be expressed in terms of instantaneous active and reactive components:

$$\begin{aligned} \vec{I}_i &= \frac{1}{2} \text{Re}\{p(\vec{r}, t)\} \text{Re}\{\vec{u}(\vec{r}, t)\} \\ &= \vec{I}_a(\vec{r}, t) + \vec{I}_{re}(\vec{r}, t) \end{aligned} \quad (2)$$

$$\vec{I}_a(\vec{r}, t) = \vec{I}(\vec{r}) \cdot [1 + \cos 2(\varphi - \omega t)] \quad (3)$$

$$\vec{I}_{re}(\vec{r}, t) = \vec{Q}(\vec{r}) \cdot \sin 2(\varphi - \omega t). \quad (4)$$

The instantaneous active acoustic intensity in (3) is seen to consist of two vectors. The first is time independent while the second is oscillatory. Conversely, the instantaneous reactive acoustic intensity vector in (4) is purely oscillatory. Time averaging of (2) results in the active intensity which represents the net transport of acoustic energy:

$$\begin{aligned} \langle \vec{I}_i(\vec{r}, t) \rangle_t &= \langle \vec{I}_a(\vec{r}, t) \rangle_t + \langle \vec{I}_{re}(\vec{r}, t) \rangle_t \\ &= \vec{I}(\vec{r}) + 0. \end{aligned} \quad (5)$$

However, the amplitude of the reactive intensity is also of interest because it represents the presence of local oscillatory energy flow. Local oscillatory energy is required to support the existence of any spatial heterogeneity in the acoustic pressure field. Equations (6) and (7) below respectively show that the active intensity amplitude is proportional to the phase gradient, while the reactive intensity amplitude is proportional to the pressure gradient.

$$\vec{I}(\vec{r}) = \frac{P^2(\vec{r})}{2\omega\rho} \vec{\nabla}\varphi(\vec{r}) \quad (6)$$



$$\bar{Q}(\vec{r}) = \frac{-1}{4\omega\rho} \bar{\nabla} P^2(\vec{r}) = \frac{-1}{2\omega\rho} P(\vec{r}) \bar{\nabla} P(\vec{r}). \quad (7)$$

Through use of the Weiner-Khintchine formula, Eq. (1) can be expressed in the spectral domain as a cross spectrum between the acoustic pressure and the acoustic particle velocity at a common point in space:

$$G_{p\vec{u}}(\vec{r}, \omega) = \frac{2}{T} E \{ P_k^*(\omega, T) \bar{U}_k(\omega, T) \}, \quad (8)$$

where  $T$  is record length,  $\omega$  is radian frequency,  $P_k(\omega, T)$  is the finite Fourier transform of the  $k^{\text{th}}$  record of the acoustic pressure, and  $\bar{U}_k(\omega, T)$  is the same for the particle velocity. The operation  $E\{\dots\}$  represents ensemble averaging over  $N$  records.

## B. Application of Intensity Processing to DIFAR Signals

SSQ-53D DIFAR sonobuoys are true *acoustic vector sensors* in that they can sense acoustic particle velocity directly in two orthogonal directions. By *adding* the output of the collocated omni-directional pressure sensor with a velocity sensor output, a cardioid receiving pattern can be formed. Taking into consideration the cardioid pattern formed by the sum of the pressure channel with the second directional sensor, the bearing of a distant source in the horizontal plane, particularly at very low frequencies, can be determined.<sup>14,15</sup> The DIFAR sonobuoy may also be used as an acoustic vector *intensity* sensor which is in contrast to current operational procedures. The equations to be used for the intensity processing of DIFAR signals are as follows.

Let the omni-directional pressure signal be  $z_p(t)$ , with Fourier transform  $Z_p(\omega) = P e^{i\theta}$ . The DIFAR sensor has two orthogonal directional transducers that sense acoustic particle velocity or acceleration. Let their Fourier components be:

$$\begin{aligned} Z_{NS}(\omega) &= V_{NS} e^{i(\theta+\alpha)} \\ Z_{EW}(\omega) &= V_{EW} e^{i(\theta+\gamma)}. \end{aligned} \quad (9)$$

Denote  $\beta$  the bearing angle of the incoming acoustic wave relative to magnetic North. We have  $V_{NS} = V \cos \beta$  and  $V_{EW} = V \sin \beta$ , where  $V$  is the vector magnitude. The cross spectra that may be formed among DIFAR channels result in the active and reactive acoustic intensity components in the respective N-S and E-W directions:



$$\begin{aligned}
I_{NS}(\omega) &= \text{Re} \left\{ \frac{2}{T} E \{ Z_p^* Z_{NS} \} \right\} = PV \cos \beta \cos \alpha \\
Q_{NS}(\omega) &= \text{Im} \left\{ \frac{2}{T} E \{ Z_p^* Z_{NS} \} \right\} = PV \cos \beta \sin \alpha \\
I_{EW}(\omega) &= \text{Re} \left\{ \frac{2}{T} E \{ Z_p^* Z_{EW} \} \right\} = PV \sin \beta \cos \gamma \\
Q_{EW}(\omega) &= \text{Re} \left\{ \frac{2}{T} E \{ Z_p^* Z_{EW} \} \right\} = PV \sin \beta \sin \gamma,
\end{aligned} \tag{10}$$

The velocity sensors in a DIFAR receiver are essentially collocated; therefore, the phase of the E-W channel is equal to that of the N-S channel,  $\alpha = \gamma$ . This phase is identical to the phase between pressure and particle velocity  $\varphi$ , which is the cross spectrum phase of Eq. (8). The active intensity magnitude is a possible detection statistic, i.e.

$$DS_I \equiv \sqrt{I_{NS}^2 + I_{EW}^2} = PV |\cos \varphi|. \tag{11}$$

From the two components of active intensity, an estimate of the bearing is computed:

$$\hat{\beta} = \tan^{-1} \left( \frac{I_{EW}}{I_{NS}} \right). \tag{12}$$

We note that the signs of  $I_{NS}$  and  $I_{EW}$  determine the quadrant of the angle  $\hat{\beta}$ ; there is no ambiguity in using Eq. (7). The detection statistics for the reactive intensity is likewise given by:

$$DS_R \equiv \sqrt{Q_{NS}^2 + Q_{EW}^2} = PV |\sin \varphi|. \tag{13}$$

Note that  $\varphi = 0$  only for plane waves and the reactive intensity is zero as expected. When the phase angle  $\varphi$  is non-zero, as would be for the case of wavefronts having curvature, the reactive intensity will be non-zero. Indeed, the phase angle itself is a viable detection statistic.

### C. Application of Intensity Processing to Forward Scattering

When there is a scattering object between a source and receiver, the scattered acoustic field and the incident acoustic field will interfere and produce a field that is rich in acoustic pressure gradients. At low frequencies, where the wavelength of sound is large compared to the typical dimensions of the scattering body, the incident sound passes by the body with little distortion; scattering is virtually absent in this so-called Rayleigh region. As the wavelength becomes comparable to the larger dimensions of the scattering body, the object scatters energy specularly. Here, the predominant scattered intensity is at an angle from the body that is approximately equal to the incidence angle of the

source-generated wavefronts (angle of reflection equals angle of incidence). As the frequency of the incident wave increases still further, and the wavelength becomes comparable to the smallest radii of curvature of the scattering body, acoustic diffraction effects appear. An acoustic shadow forms in the forward-scattered direction due to the severe interference between the incident and scattered wave fields. This shadow forms regardless of the incident sound pulse length, or angle of incidence. In the forward-scattered direction, the incident wave and the scattered wave interfere over essentially the same time scale because there is virtually no difference in path length between the two fields. Thus, it makes no difference in the forward direction whether the source is operated steady state, or is impulsive.

From Eq. (7), the reactive vector intensity is seen to be directly proportional to the product of pressure and pressure gradient. The predominant pressure gradients in the forward-scattered direction are perpendicular to the boundaries of the shadow. Thus, the reactive intensity component that is in these directions might be a reliable indicator of the presence of the object. Equation (13) suggests that the cross-spectral phase angle (or the sine of this angle) between the acoustic velocity component in this direction and the acoustic pressure may also be a reliable indicator of the object.

Exact formulations and computations<sup>10-13</sup> were performed for the intensity field scattered by a 10:1 fineness ratio rigid prolate spheroid. Figure 1 shows the computed scattered pressure and total pressure (incident plus scattered) beam patterns for the prolate spheroid insonified by a plane wave incident at  $60^\circ$  to the major axis of the spheroid. The right-hand part of this figure shows clearly that the total scalar pressure field is dominated by the incident field. The perturbation in the forward-scattered pressure field is less than 0.5 dB. The intensity field shows a more definitive result.

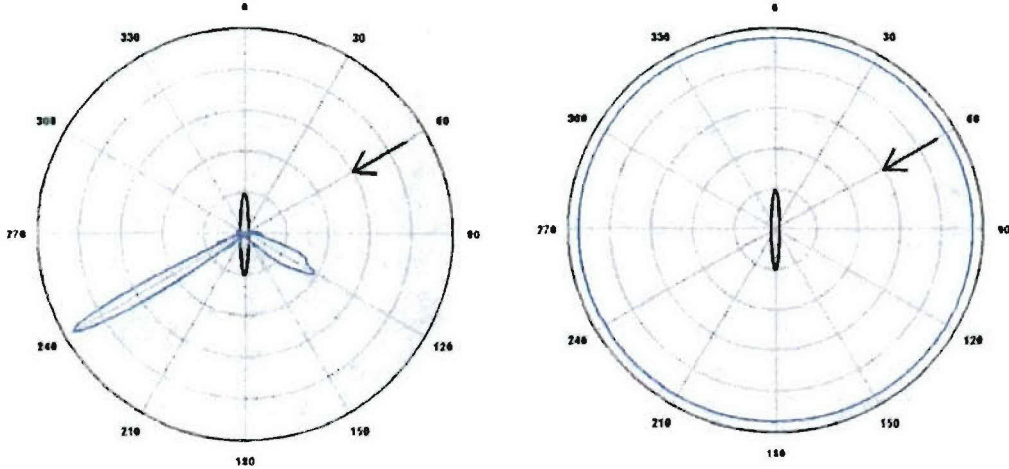


Figure 1. Beam pattern of the scattered pressure (left) and total (incident plus scattered) pressure (right) for a 10:1 fineness ratio, rigid prolate spheroid insonified by a plane wave at  $60^\circ$  incidence.<sup>10-13</sup> The incident field masks the scattered pressure. The reduced frequency for these computations is  $kd/2 = 33.3$ , where the acoustic wavenumber is  $k$  and the interfocal distance of the spheroid is  $d$ .



The pressure-velocity component phase (or reactive intensity component) in a direction transverse to the incident wave vector is the component that is proportional to the most severe pressure gradients in the forward scattered region. A typical field plot of the phase of the transverse component of intensity is given in Fig. 2. This plot covers about 15 body lengths in any direction from the scattering spheroid, and the body is 12.75 acoustic wavelengths long. These results provide theoretical evidence that intensity-based processing may help solve the forward-scattered occlusion zone problem through measurement of the phase variations in the total acoustic field.

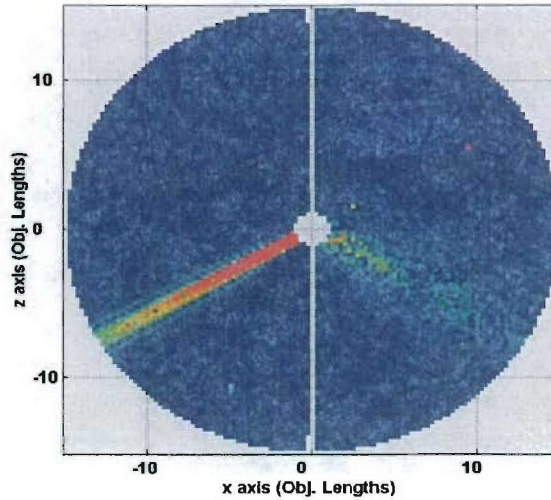


Figure 2. Computed phase field for the intensity component that is transverse to the incident plane wave propagation vector which insonifies a 10:1 fineness ratio, rigid prolate spheroid at  $60^\circ$  to the major axis.<sup>10-13</sup> The major axis of the spheroid is oriented vertically, and the incident wave originates in quadrant 1. The reduced frequency is  $kd/2 = 40$ .

### III. EXPERIMENTAL STUDIES OF FORWARD SCATTERING

In this section we will describe two test programs involving the use of SSQ-53D DIFAR sonobuoys in detecting large bodies in forward scatter. The first test took place in April 2004 at the Naval Undersea Warfare Center, Seneca Lake Sonar Test Facility at Dresden, NY. The objectives of this first test program were to verify that DIFAR sonobuoys could be used as underwater acoustic intensity sensors, and to explore their use in detecting an object in the forward-scattered occlusion zone. Only one useful run was accomplished because of some logistical issues involving another test program being conducted by another organization at the facility during the same time period as the subject test. In May 2005, a more thorough test program was conducted at the Naval Surface Warfare Center, Lake Pend Oreille Acoustics Research Detachment at Bayview, ID. The objective was to continue the work begun at Seneca Lake, but with a larger scattering body, with the source operating over a broad range of frequencies, and with several receivers in the line-of-sight.

### A. Seneca Lake Test Program

The sensors used in the Seneca Lake experiments were standard SSQ-53D DIFAR sonobuoy hydrophone assemblies. These directional hydrophone assemblies generate a multiplexed signal that may be either hardwired to the lab or linked by RF using the standard DIFAR transmitter. Figure 3 shows one of these sensors, which is approximately 10 cm in diameter by 25 cm long.

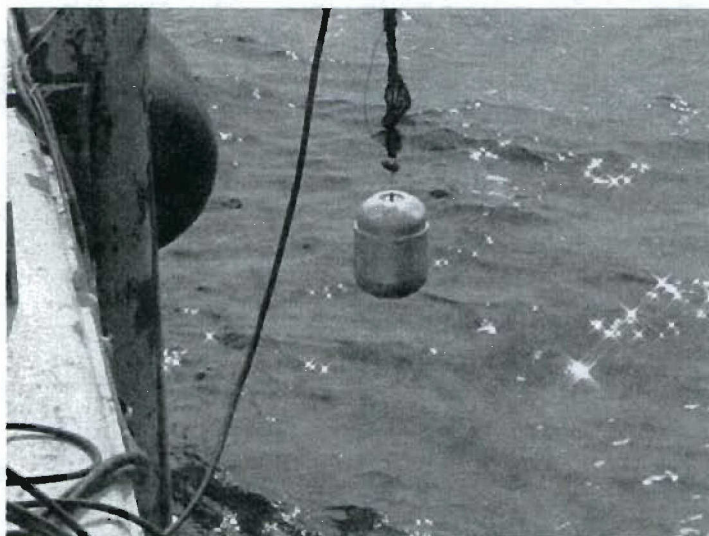


Figure 3. Photograph of the directional sensor of a SSQ-53D DIFAR sonobuoy. The unit is negatively buoyant and is suspended by its signal cable exiting the top-side of the case.

Surface-float assemblies were designed to replace the inflatable float of a standard sonobuoy. The design is basically a spar buoy which provides significant vertical direction stability due to wave motion. They were fabricated from long sections of PVC pipe, which also house the battery power supply, transmitter, and antenna for the RF link. Non-rechargeable alkaline D-cell batteries were used for convenience. Their useful life was in excess of 20 hours. The DIFAR transmitters are all 99-channel electronic function select units; however, to minimize interference from recreational sources, operations were limited to channels 2-16, 18-31, and 31-47. Figure 4 shows a photograph of one of these floats in the lake. The vertical yellow element is the RF antenna. The copper strip on the side of the float that enters the water is a ground strap that is hardwired to the sensor case.

The acoustic source, provided by the Seneca Lake facility, was excited in the 500 to 2,400 Hz frequency band. A 2,048 Hz pure-tone pulse, 5 ms long repeated every 0.5 s was used in the forward-scattering test. The DIFAR receiver had zero electronic phase mismatches among the two directional channels and the omni-directional pressure channel (omni channel) at the selected frequency. This was determined by exciting the water volume with continuous broadband noise in the band noted above and measuring the cross spectra among the various channels of the DIFAR sensor.





Figure 4. Photograph of the surface float from which the DIFAR sensor is suspended at a prescribed depth. It also contains the multiplexer, FM transmitter, and batteries.

An FM receiver system is required for the RF-linked signals from the DIFAR transmitters. Both a 31-channel ARR-75 sonobuoy receiver system and a 99-channel ARR-84 sonobuoy receiver system were available from the Naval Air Warfare Center, Aircraft Division located at Patuxent River, MD. These receivers were set for  $2 V_{\text{rms}}$  for 75 kHz deviation. DIFAR de-multiplexers, manufactured by Sparton, were used for separation of the omni and the two directional sensor outputs. These signals were recorded on a TEAC digital tape recorder. Various cross- and auto-spectra were then performed on the tapes using an Agilent Model 35670A four channel digital signal analyzer (DSA) using 128 spectral averages.

A schematic of the source, target, and receiver positions is given in Fig. 5. Figure 6 shows a photograph of the target which is 5.8 m long. The reduced frequency based on body length (not interfocal distance because the body is not a prolate spheroid) is  $h = kL/2 \approx 25$ .

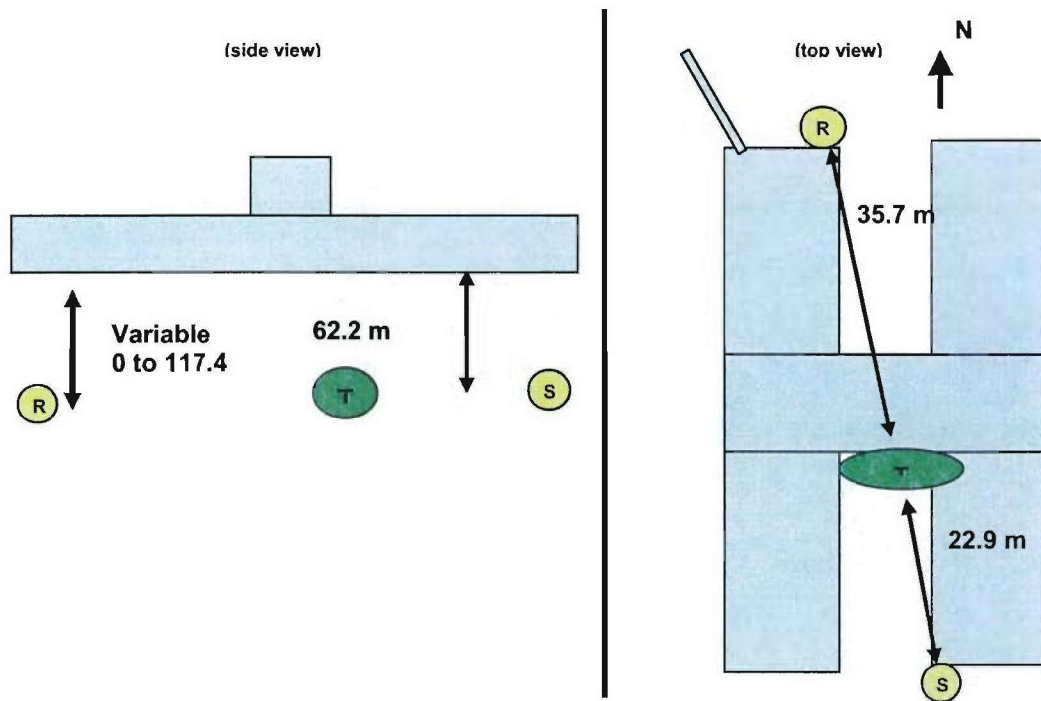


Figure 5. Diagram of the Seneca Lake Systems Measurement Platform, and the relative positions of the source, receiver, and target used in the forward scattering tests.



Figure 6. Photograph of the Seneca Lake scattering body (target).

In the forward-scattering experiment, the receiver was secured to a wench cable located on the North end of the System Measurement Platform. The water depth at this

location is 144.8 m. The sensor was systematically lowered in a stop-start fashion from a depth of 45.7 m to 117.4 m in increments of approximately 1.22 m. During the pauses in the traverse, 120 pings of data were collected. As noted in Fig. 5, the source, target, and receiver would be in line at a depth of 62.2 m. The mean-square pressure level measured by the omni phone in the DIFAR sensor during the sensor traverse is given as a function of depth in Fig. 7. Note that the slight perturbation in pressure in the line of sight is of comparable magnitude to that predicted and shown in the right-hand graph of Fig. 1.

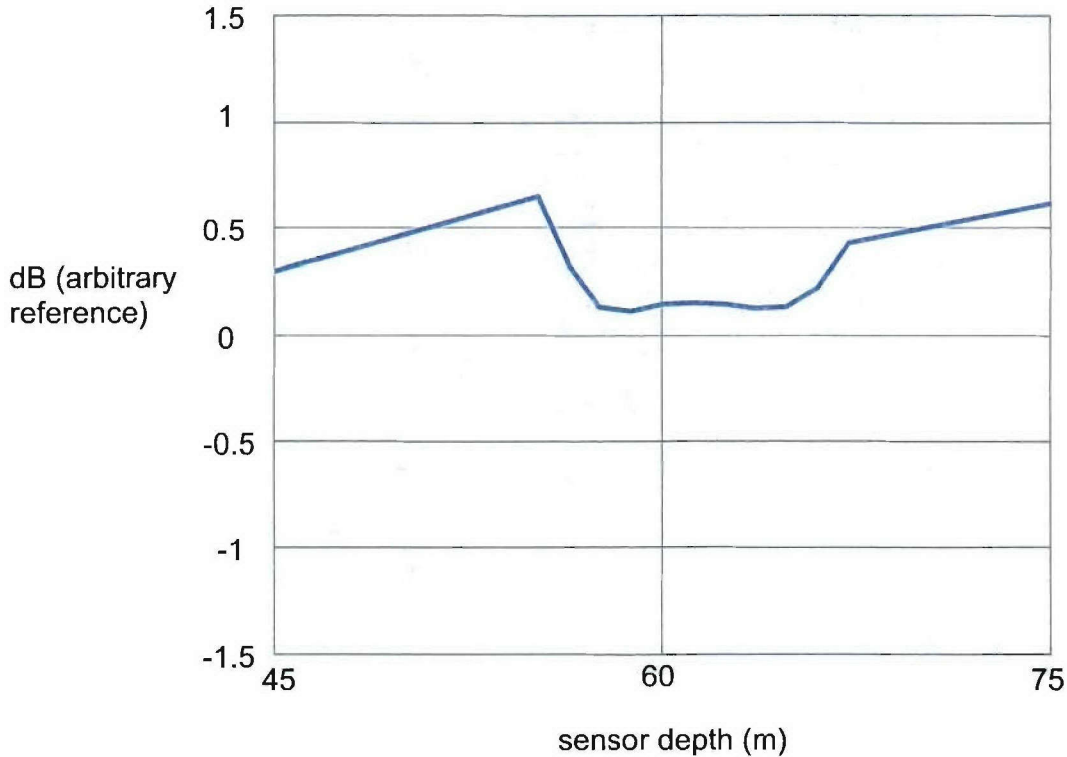


Figure 7. Variation of the acoustic pressure during the traverse of the sensor through the line of sight which is at a depth of 62.2 m.

At each increment of the sensor traverse, two cross spectra were measured: one between the E-W directional channel and the omni channel, and the other between the N-S channel and the omni channel. Of interest is the phase angle of these cross spectra which correspond to  $\phi(\vec{r})$  in the equations of Section II. Now the Systems Measurement Platform is aligned in a North-South direction, so the intensity component obtained from the cross spectrum of the N-S channel with the omni channel is in the direction of the incident wave. Likewise, that obtained with the E-W channel is perpendicular to the direction of the incident wave. Figure 8 shows the cross spectral phase for these two components of intensity. Clearly, the phase corresponding to the perpendicular component shows a strong perturbation – as much as  $60^\circ$  – as the sensor passes through the line of sight connecting source and target. The N-S component does not have this



perturbation. Both trends are predicted by the calculations.<sup>10-13</sup> This single dataset suggests that the intensity processing of the DIFAR signals may lead to a target detection in the occlusion zone; however, the range from target to receiver is not significantly large, so many additional experiments are required before firm conclusions can be made.

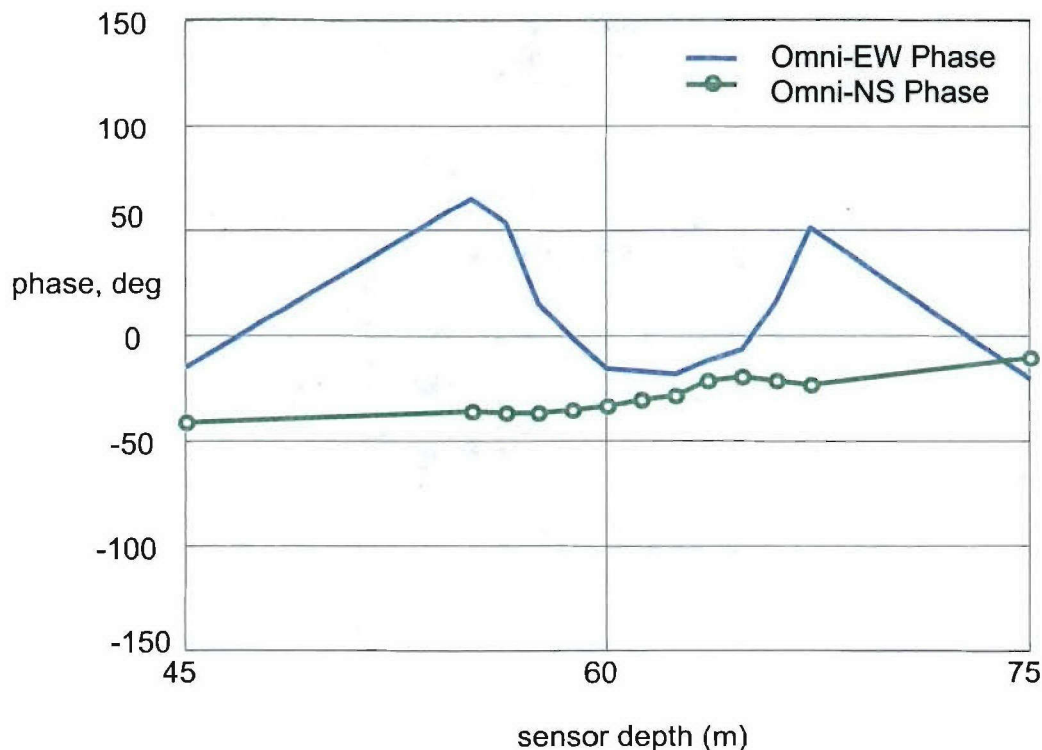


Figure 8. Variation of the E-W component and the N-S component of the intensity phase during the traverse of the sensor through the line of sight which is at a depth of 62.2 m.

## B. Lake Pend Oreille Test Program

This test program was conducted on the Intermediate Scale Measurement System (ISMS) range, which is located on Lake Pend Oreille approximately 11 miles north of Bayview, ID. The water depth at this site is 350 m. The scattering body is a 2.44 m diameter cylinder, 19.2 m long with hemispherical endcaps, Fig. 9. An ITC 4141 spherical source (Fig. 10) was secured from the ISMS barge at the test depth of 123 m. The source was approximately 30 m (10 acoustic wavelengths at 500 Hz) from the target; thus, the incident waves are considered planar. The source was driven with white noise in the 500 to 3,200 Hz frequency band.

Four (4) SSQ-53D DIFAR sensors were prepared for use as intensity receivers. They were positioned in line with the source; the body was hoisted up and down through this line-of-sight. Figure 11 shows a schematic of the experimental setup. The sensors





Figure 9. Photograph of the target used in the forward-scattering experiments at Lake Pend Oreille.

are labeled *A* through *D*, with *A* being the closest to the target at a range of  $R_1 = 5L$ , where  $L$  is the body length. The range of sensor *B* is  $10L$ , that of *C* is  $20L$ , and *D* is located at the farthest range tested,  $30L$ . The top-side buoys were re-designed versions of the ones used at Seneca Lake. Some of the details are given in Fig. 12. Each of the four receivers operated on a different radio frequency so that their signals could be received and processed independently of each other. Figure 13 shows a photograph of the deployed line array of surface floats. The floats were fastened to a taught line connecting the test barge with a remote platform anchored to the bottom by two opposing anchors. The line was purposely aligned in the magnetic N-S direction so that the radial and transverse components of acoustic intensity could be measured directly, without correction for sensor orientation.



Figure 10. The ITC 4141 spherical source used in the Lake Pend Oreille scattering test.

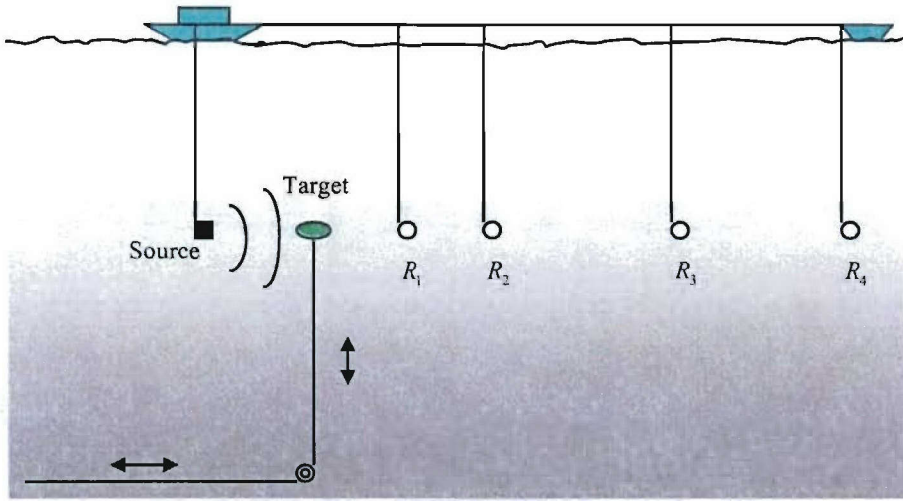


Figure 11. Schematic diagram of the scattering experiment performed at Lake Pend Oreille. The source and line array of receivers are at a depth of 123 m.

The un-calibrated acoustic intensity phase data from two different scattering experiments will now be presented. In the first, the target was lowered through the line-of-sight. The nominal angle of incidence made between the plane wave vector and the axis of symmetry of the body was  $90^\circ$ . The independent variable for the forward scattering results in this case is the target depth. In terms of the prolate spheroidal coordinates used in the Rapids and Lauchle calculations<sup>10-13</sup> this would correspond to variations in the  $\phi$ -variable which is the angle of rotation about the major axis of the spheroid. Those calculations – and others<sup>4</sup> – indicate that the variability of the scattered field is relatively weak in variation with this coordinate.

In the second experiment, the target was secured at the same depth as the source and receivers. The source was then manually moved laterally along the ISMS barge to affect a change in the incidence angle. The source position (latitude and longitude) was determined from GPS readings. Because the receiving array was fixed in space, the net result is a variation in the bearing angle of the scattered energy in the plane of the major features of the body. In terms of the spheroidal calculations, this would correspond to changes in the  $\eta$ -coordinate at constant  $\phi$ , with each receiver at a different value of  $\xi$ .

### 1. Descending Target Test

Figures 14–17 show the un-calibrated acoustic pressure measured in the first experiment where the target was lowered through the line-of-sight. This pressure variable is simply the output auto-spectral level of the omni-channel voltage, corrected for the frequency response of the source (known). It is presented as a function of the non-dimensional frequency  $h = kL/2$  on one axis of the 3-D plot, and as a function of target depth on the other axis. We note that for all four sensors, only a small perturbation ( $< 1$  dB) in the pressure signal appears as the target passes through the line-of-sight. These results show clearly the problem of detecting a target in the forward-scattered occlusion zone using a scalar pressure sensor. The results support Figs. 1 and 7 also.

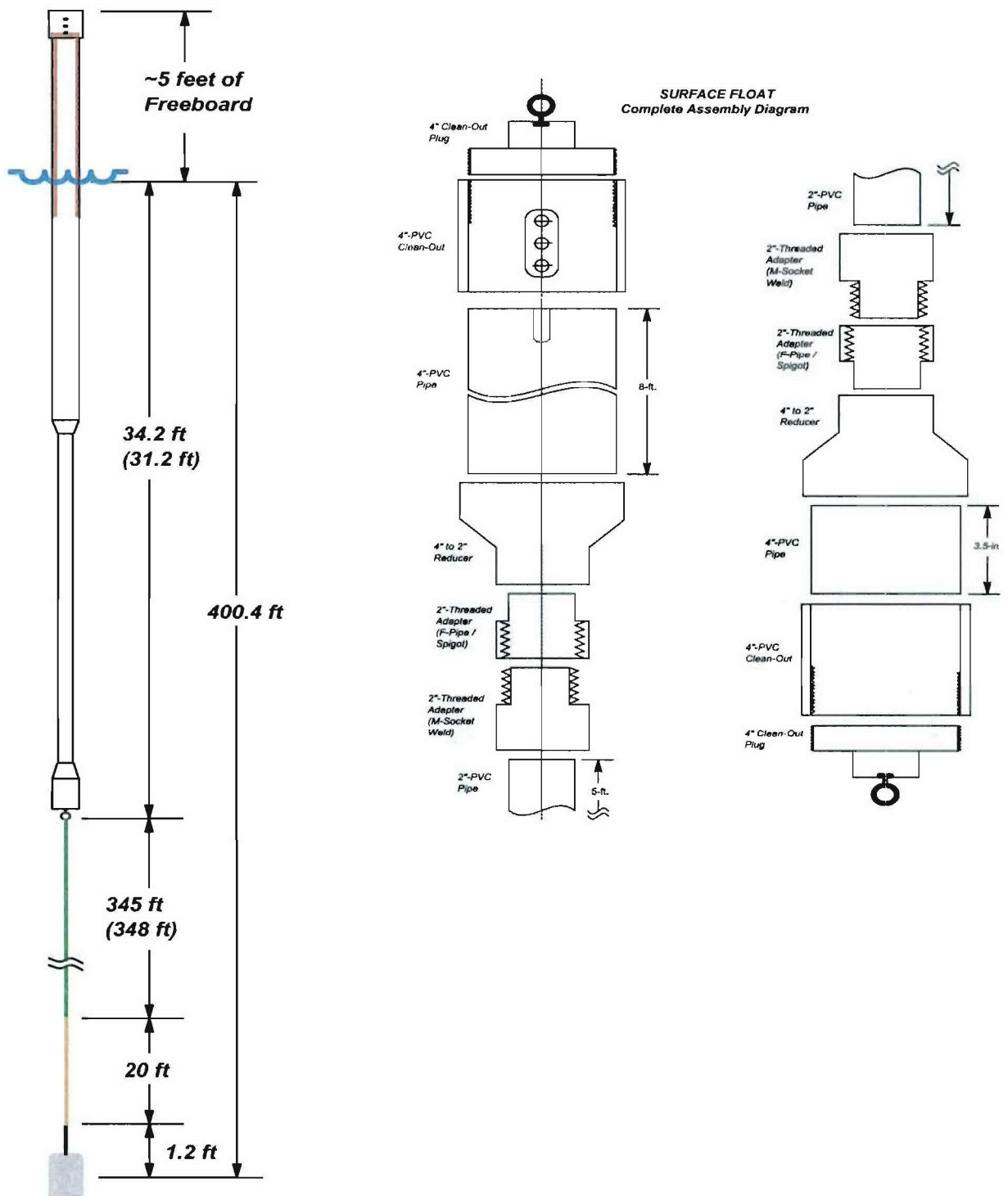


Figure 12. Details of the top-side spar buoy that supports the intensity sensor at depth, while containing the D-cell battery power pack, multiplexer, and FM radio transmitter.



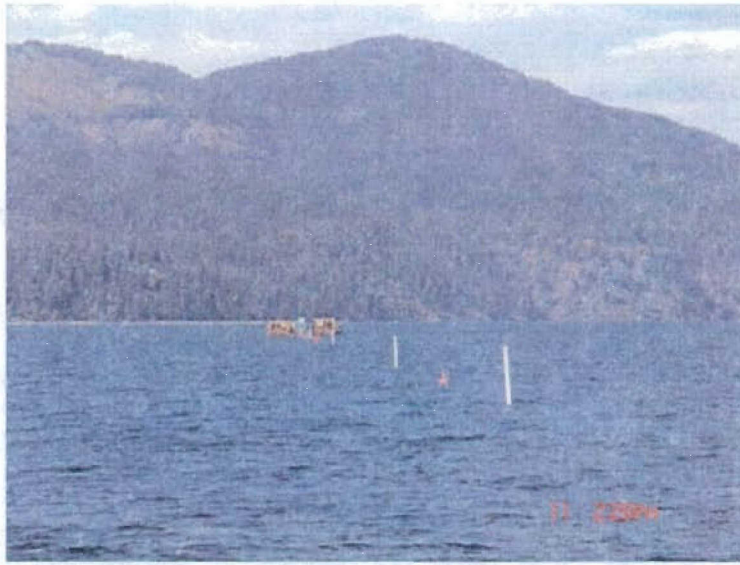


Figure 13. Photograph of the deployed array of surface floats, each supporting an individual DIFAR sensor at 123 m depth.

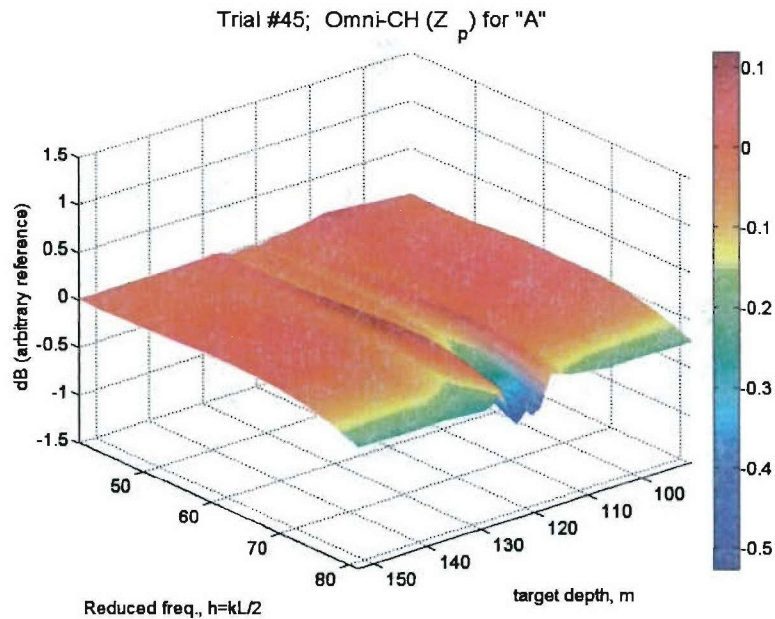


Figure 14. Auto-spectra of the sensor *A* omni-channel voltage measured as the target was lowered through the line-of-sight at 400 ft (123 m).

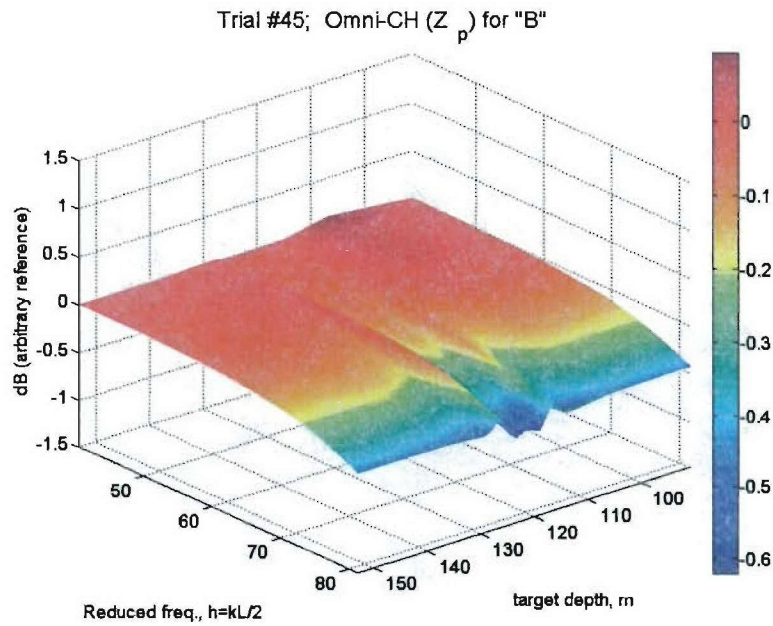


Figure 15. Auto-spectra of the sensor *B* omni-channel voltage measured as the target was lowered through the line-of-sight at 400 ft (123 m).

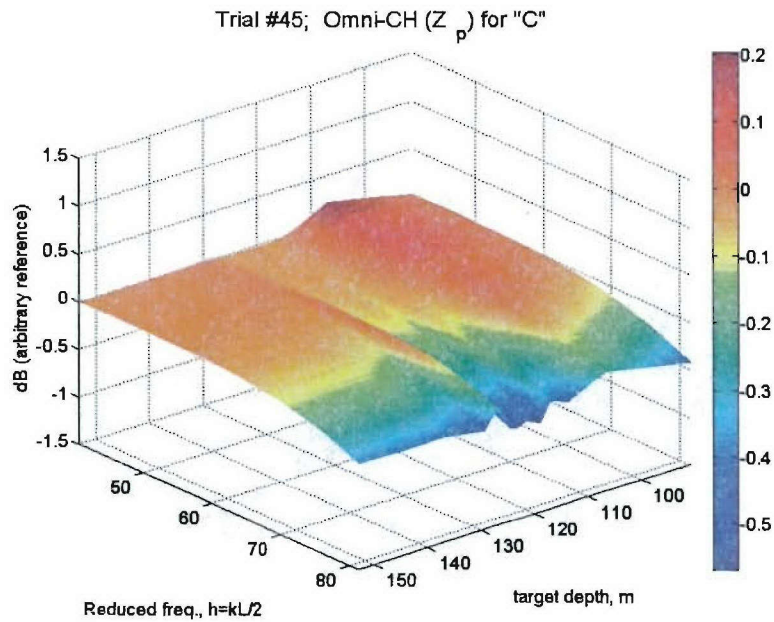


Figure 16. Auto-spectra of the sensor *C* omni-channel voltage measured as the target was lowered through the line-of-sight at 400 ft (123 m).

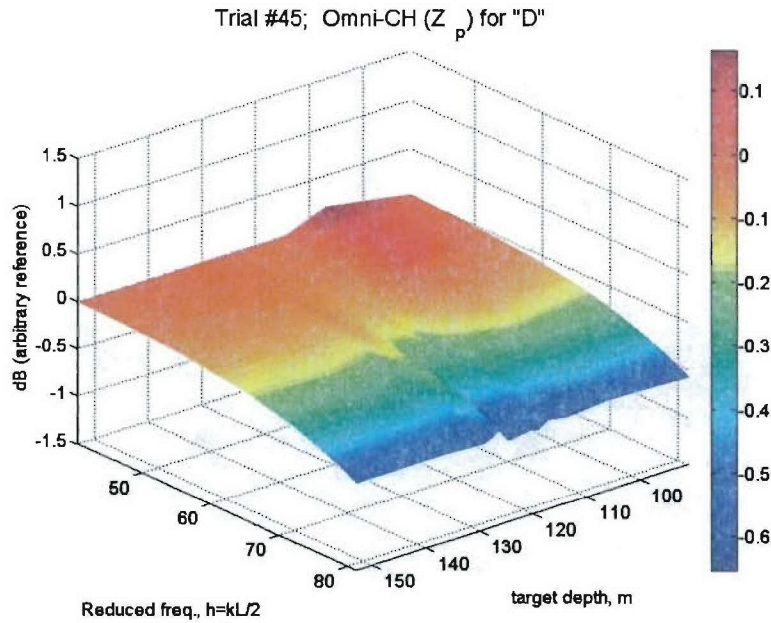


Figure 17. Auto-spectra of the sensor *D* omni-channel voltage measured as the target was lowered through the line-of-sight at 400 ft (123 m).

In the next group of figures (Figs. 18-21), the phase of the cross spectrum measured between the omni-channel and the N-S directional channel is presented as a function of frequency and target depth. This component of phase corresponds to the component of intensity phase in the direction of the incident wave ( $\xi$  – direction in the spheroidal calculations<sup>10-13</sup>). There are no calibrations applied to these phase plots, although a constant was applied to each phase spectrum so that the presented results have a mean value of  $0^\circ$  across the frequency range. There is some observed sensor/electronic phase mismatch and other secondary phase variation due to environmental conditions present in these plots. These effects may be seen in the spectra presented at the extreme values of depth [300 ft (91 m) and 500 ft (152 m)]. At these depths, the target is well out of the direct line-of-sight of the received signal, which is essentially composed of the direct plane wave signal created by the source, and perturbations due to bottom and surface reflections. Recall that a steady-state random noise signal was used to drive the source in all of these tests. The full effects of lake reverberation are thus included in the presented data. The figures reveal a very small phase variation ( $\pm 10^\circ$ ) as the target passes through the line-of-sight. Again, the trends observed in Figs. 18-21 are consistent with the spheroidal scattering calculations and with the data of Fig. 8.



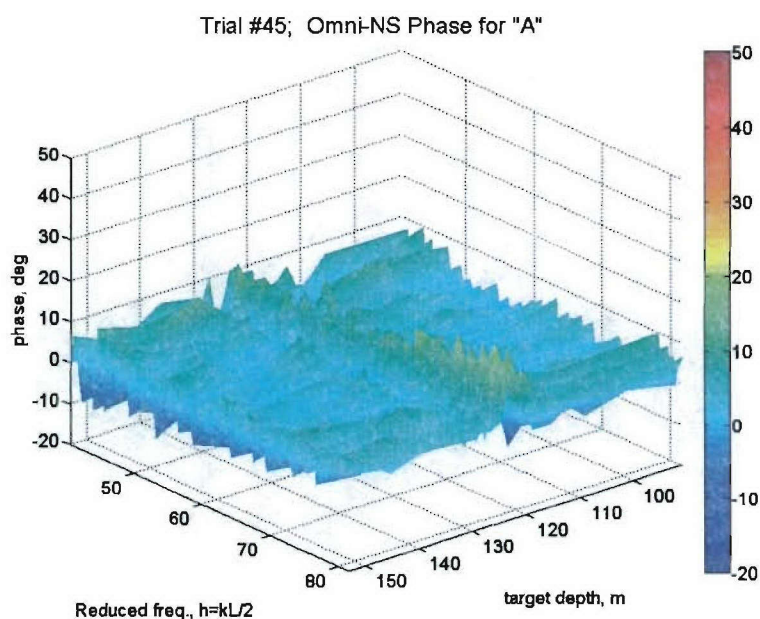


Figure 18. Cross-spectral phase spectra measured between the omni-channel and the N-S directional channel for sensor *A* as the target drops through the line-of-sight at 400 ft (123 m).

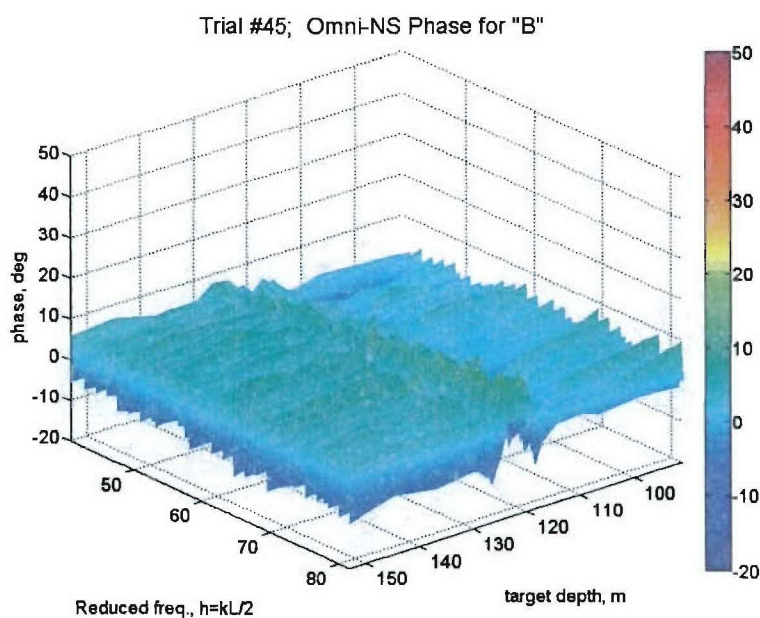


Figure 19. Cross-spectral phase spectra measured between the omni-channel and the N-S directional channel for sensor *B* as the target drops through the line-of-sight at 400 ft (123 m).

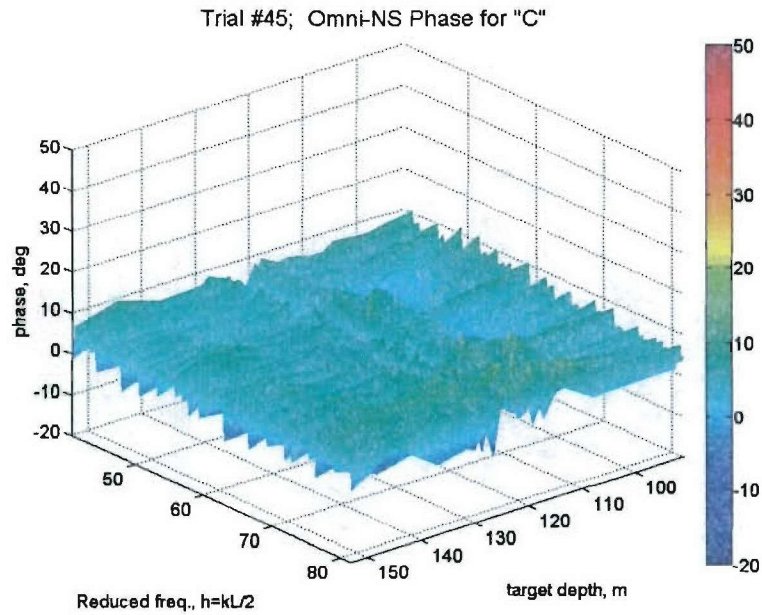


Figure 20. Cross-spectral phase spectra measured between the omni-channel and the N-S directional channel for sensor *C* as the target drops through the line-of-sight at 400 ft (123 m).

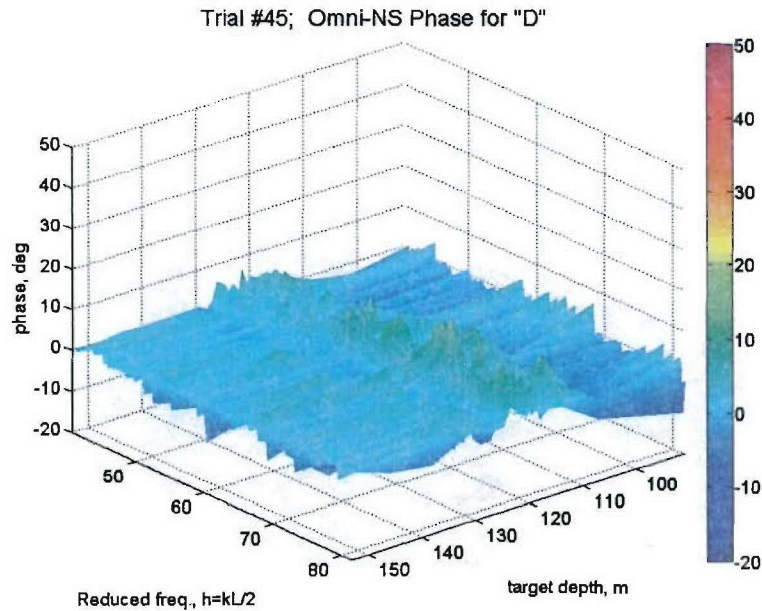


Figure 21. Cross-spectral phase spectra measured between the omni-channel and the N-S directional channel for sensor *D* as the target drops through the line-of-sight at 400 ft (123 m).



We now turn our attention to the phase of the transverse component of intensity. In these experiments, this component is determined from the phase of the cross spectrum measured between the omni-channel and the E-W directional channel. Again, no calibrations are applied in the following results, but each phase spectrum is shifted so that its mean value is  $0^\circ$  over the frequency range. Figures 22-25 show the measured data, presented in the same format as the N-S channel/omni-channel phase data.

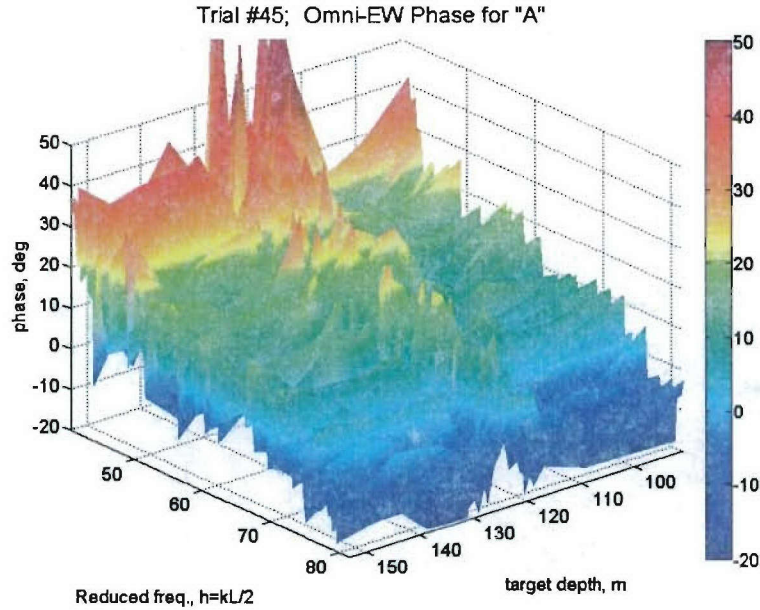


Figure 22. Cross-spectral phase spectra measured between the omni-channel and the E-W directional channel for sensor *A* as the target drops through the line-of-sight at 400 ft (123 m).

As illustrated, noticeable phase variations occur at all sensor locations as the target approaches the line-of-sight, and as it descends below the line-of-sight. This is revealed by the “double-hump” features in the 3-D plots; such a feature is also observed in the Seneca Lake experiment (Fig. 8). For these cross spectra, the expected phase shifts were projected to be larger than that measured. This is most likely due to the fact that for this configuration, the receiver does not precisely coincide with the forward-scattering line connecting the source and target. The free floating nature of the receivers and undetermined sub-surface currents make alignment in the horizontal plane problematic.

Further, the severe phase variations for  $h < 50$  in Fig. 22 are suspected of being due to acoustic saturation of the sensors in buoy *A* due to its close proximity to the source. The de-multiplexer has an indicator light that warns of over saturation. This light was observed to be intermittently on and off for sensor *A*.

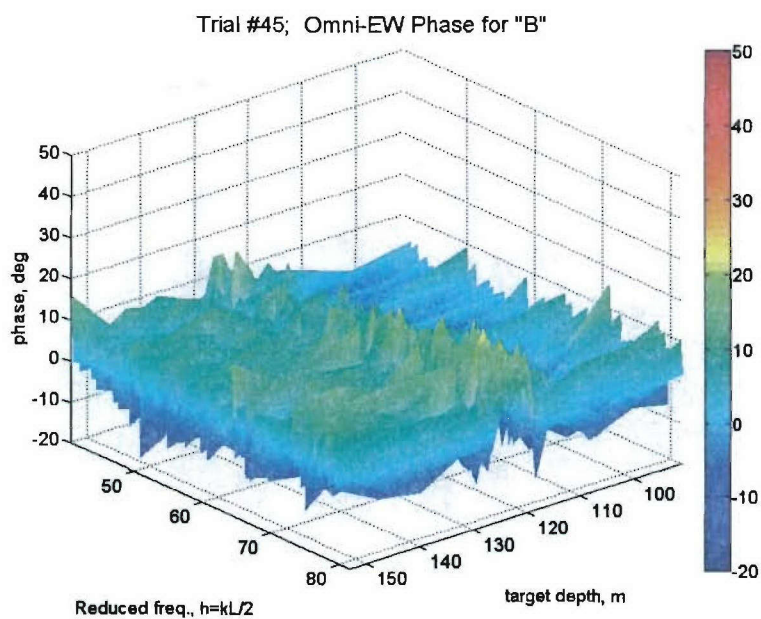


Figure 23. Cross-spectral phase spectra measured between the omni-channel and the E-W directional channel for sensor *B* as the target drops through the line-of-sight at 400 ft (123 m).

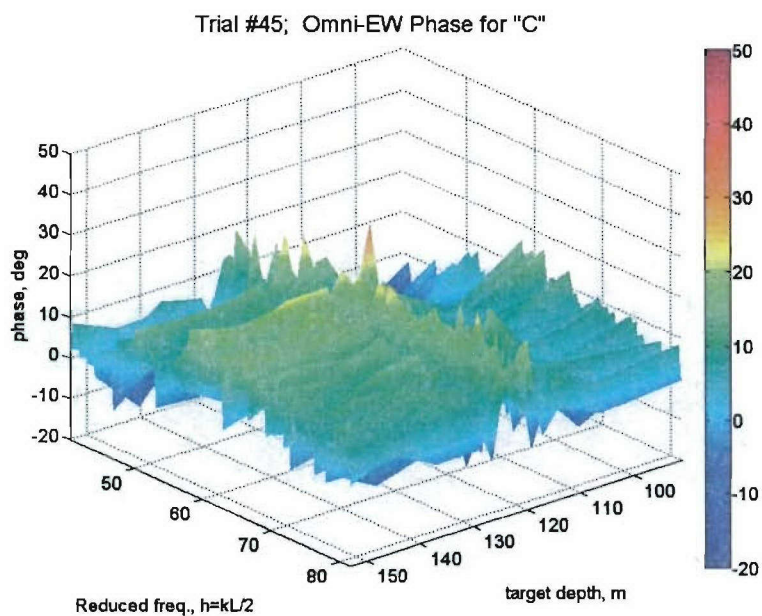


Figure 24. Cross-spectral phase spectra measured between the omni-channel and the E-W directional channel for sensor *C* as the target drops through the line-of-sight at 400 ft (123 m).



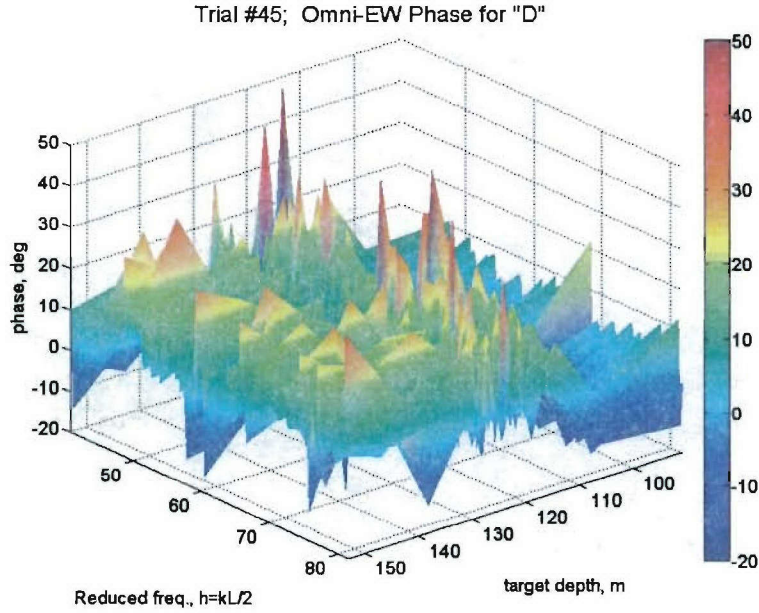


Figure 25. Cross-spectral phase spectra measured between the omni-channel and the E-W directional channel for sensor *D* as the target drops through the line-of-sight at 400 ft (123 m).

## 2. Source Sweep Test

It is desirable to conduct a forward-scattering experiment where the source, target, and receivers are all at the same depth, with the bearing of the receive array (relative to the center of the target) being the independent variable. The results of such a test would fit the format of most of the scattered intensity field calculations,<sup>10-13</sup> an example of which is presented in Fig. 2. At Lake Pend Oreille, we attempted to systematically move the remote barge that anchored one end of the line that secured the four buoys. Unfortunately, severe wind and other issues forced us to abandon this attempt.

The alternative approach was to incrementally move the source along the South side of the ISMS barge, which was very stable in the water. The receive array remained fixed in a magnetic N-S direction. GPS readings were taken at each top-side buoy location, in addition to the fifteen source positions considered. A plan view diagram of a few of the resulting lines-of-forward scatter is given in Fig. 26. The procedure provides a distinct range of forward-scatter bearings ( $\sim 20^\circ$  included angle), with  $0^\circ$  corresponding to the line-of-sight containing the receiver array. However, the target angle of incidence also changes as the source is moved. Because the prolate spheroidal calculations show strong phase changes in the forward-scattered direction, regardless of incidence angle, no attempt was made to correct any of the data for actual changes in the incidence angle. In future tests, the target could be rotated a pre-determined amount to eliminate this problem. That was not possible in the present test because the plot of Fig. 26 was not available beforehand. The multiplexed signals broadcast from buoy *A* in this source sweep experiment were saturated by an apparent high source level; therefore, the processed data for sensor *A* are not presented in the following figures.

## Bearing Angles (re. $N_{mag}$ ) with Source Sweep

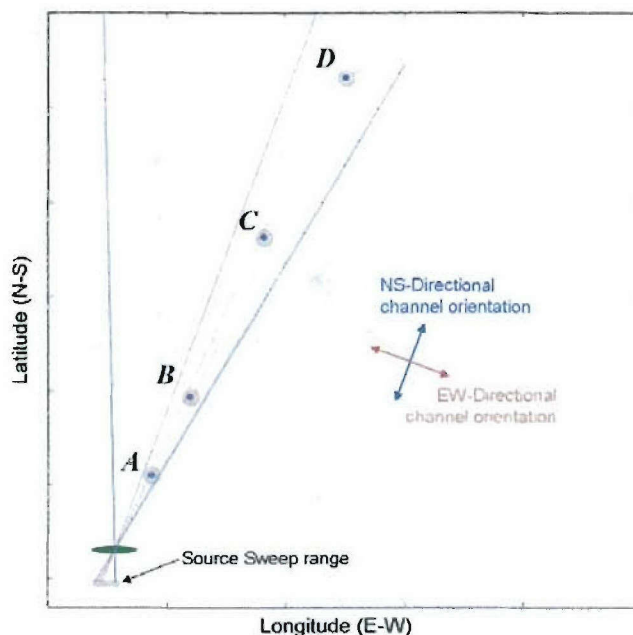


Figure 26. Shown here are the lines-of-forward scatter due to the sweeping of the source along the ISMS barge in the E-W direction (not drawn to scale).

The omni pressure spectra as a function of forward-scan bearing angle for each of the sensors *B*, *C*, and *D* are given in Figs. 27-29, respectively. As expected, there is no apparent detection of the target by any of the sensors at  $0^\circ$  which corresponds to the line-of-sight connecting source, target, and receivers.

Figures 30-32 show the phase of the cross spectrum measured between the omni-channel and the N-S directional channel presented as a function of reduced frequency and bearing angle of the forward-scan direction. Again, this component of phase corresponds to the component of intensity phase in the direction of the incident wave. The data presented in these figures indicate no discernable features that would suggest the presence of the target. We note a disturbance in the phase in Fig. 32 for  $40 \leq h \leq 50$  and for a target bearing of roughly  $-6^\circ$ . The source of this disturbance has never been conclusively confirmed, but a possible cause of it may be false scattering off the submerged rigging on the ISMS range. Except for these few isolated spikes, the phase is essentially constant for all angles and all frequencies. This indicates direct wave propagation from the source. The data support completely the trends predicted<sup>10-13</sup> for this component of scattered intensity.

Figures 33-35 present the phase spectra measured between the E-W directional channel and the omni-pressure channel of sensors *B*, *C*, and *D* for the range of bearing angles considered. Just as the data of Figs. 22-25 indicate the presence of the scattering body in the occlusion zone, these data do also. Clearly the transverse component of intensity phase is a viable indicator of the target in the occlusion zone.



The observation that the largest effect is in the phase of the orthogonal velocity/pressure cross-spectrum seems to make sense. For a traveling wave, the relative phase should be zero. The scatterer makes small changes in the magnitude and direction of the field components. Compared to the incident direction, these changes are small in that the along-axis propagation is still primarily traveling. But perpendicular to the axis, there is no component in the absence of the scatterer. The scatterer perturbs the direction of the wave – to the right for parts of the wave that pass to the right of the scatterer and to the left for parts of the wave that pass to the left of the scatterer. The transverse components lead to standing-wave-like fields, but only in the transverse direction.

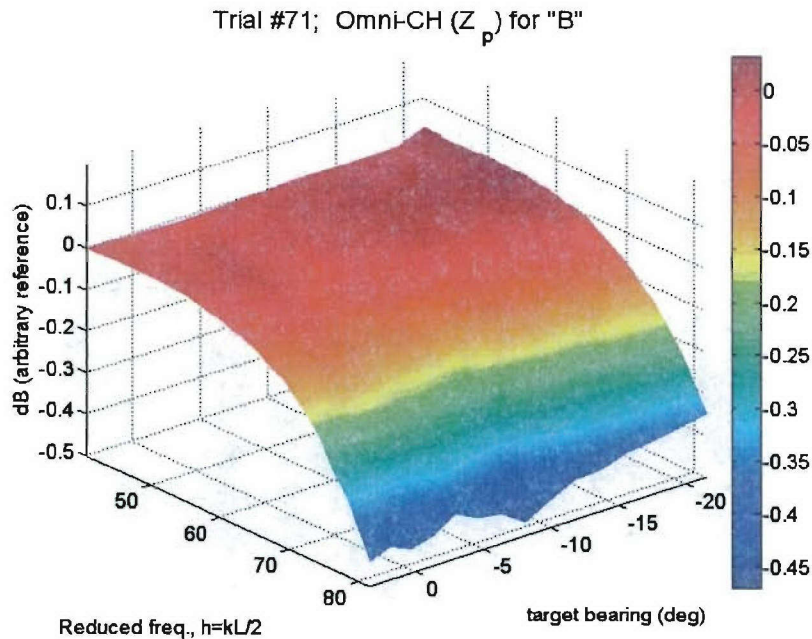


Figure 27. Auto-spectra of the sensor *B* omni-channel voltage measured as the forward-scatter bearing angle changes due to lateral movement of the source.

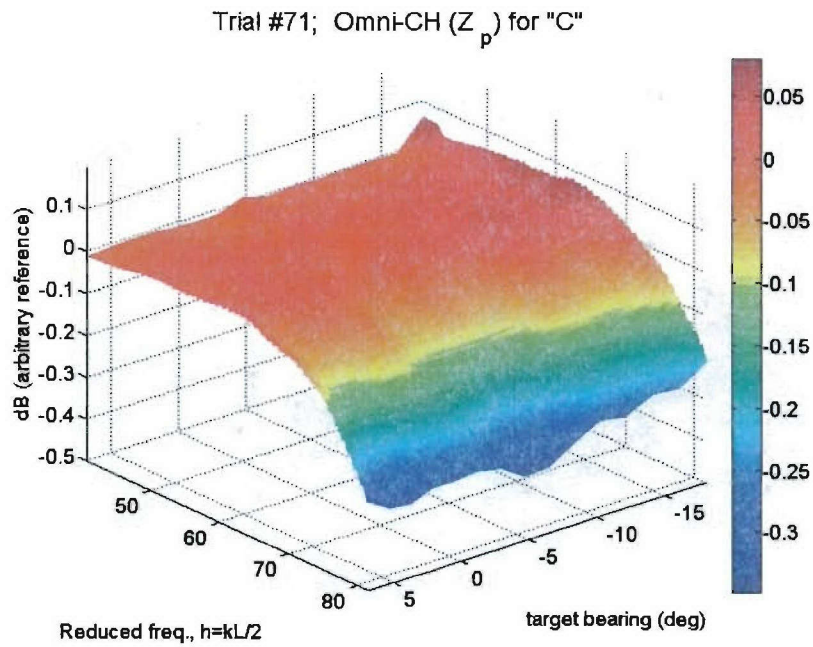


Figure 28. Auto-spectra of the sensor *C* omni-channel voltage measured as the forward-scatter bearing angle changes due to lateral movement of the source.

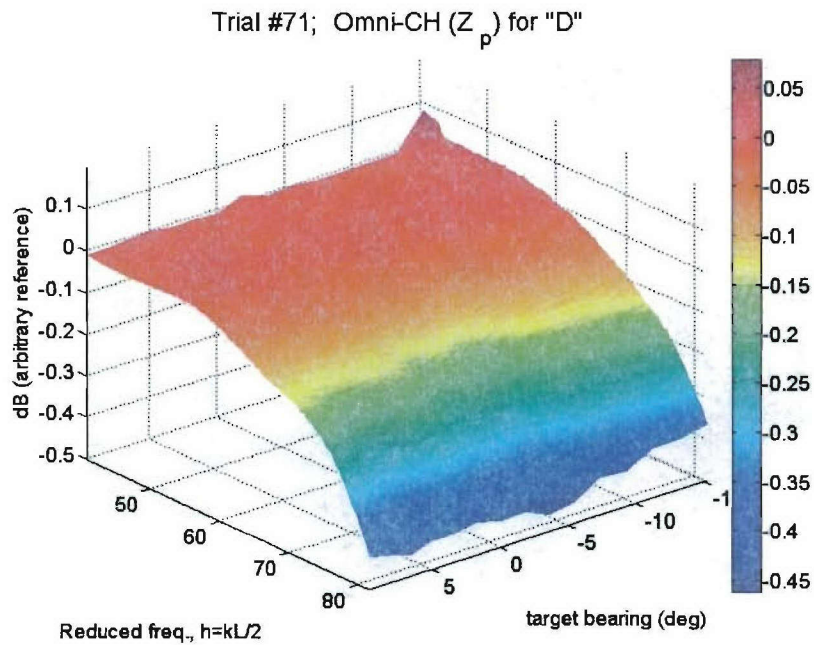


Figure 29. Auto-spectra of the sensor *D* omni-channel voltage measured as the forward-scatter bearing angle changes due to lateral movement of the source.

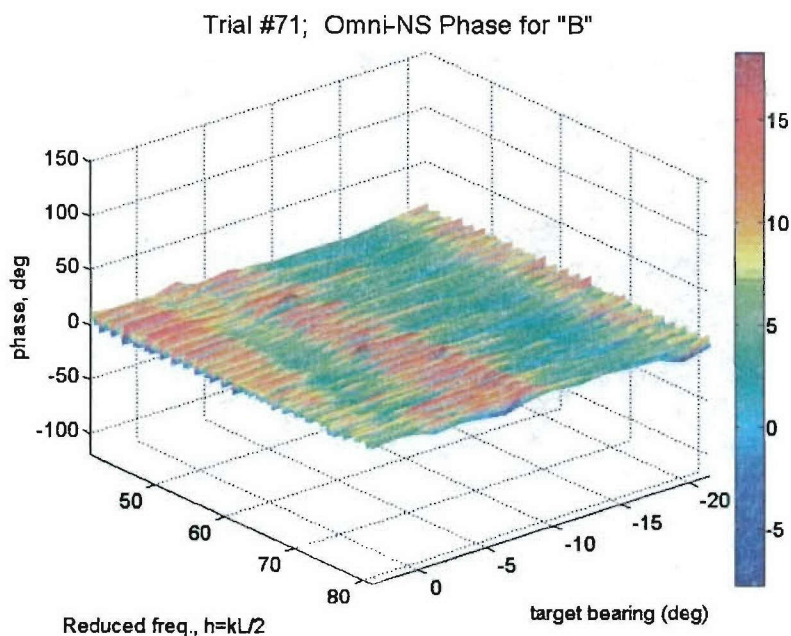


Figure 30. Cross-spectral phase spectra measured between the omni-channel and the N-S directional channel for sensor *B* as the source sweeps out the forward-scattering angles indicated on one of the abscissas. The sensor is along the  $0^\circ$  bearing.

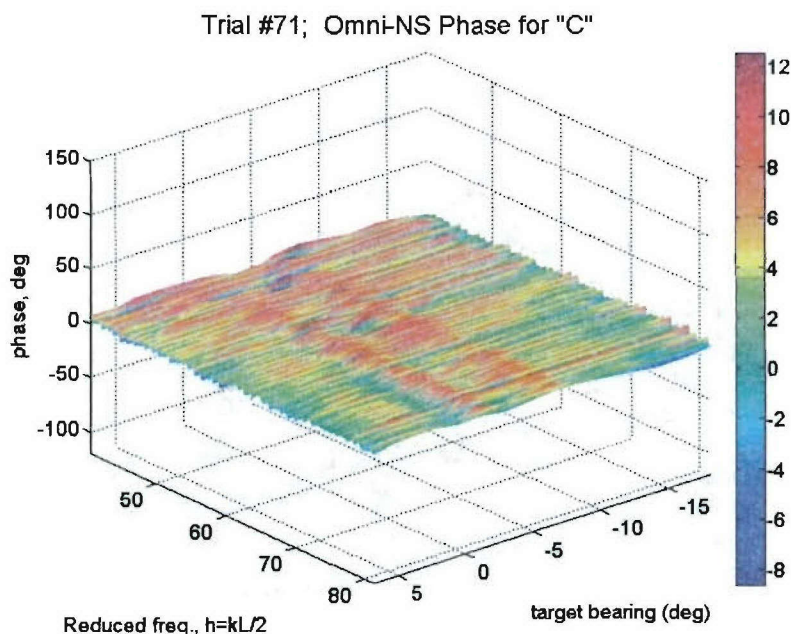


Figure 31. Cross-spectral phase spectra measured between the omni-channel and the N-S directional channel for sensor *C* as the source sweeps out the forward-scattering angles indicated on one of the abscissas. The sensor is along the  $0^\circ$  bearing.



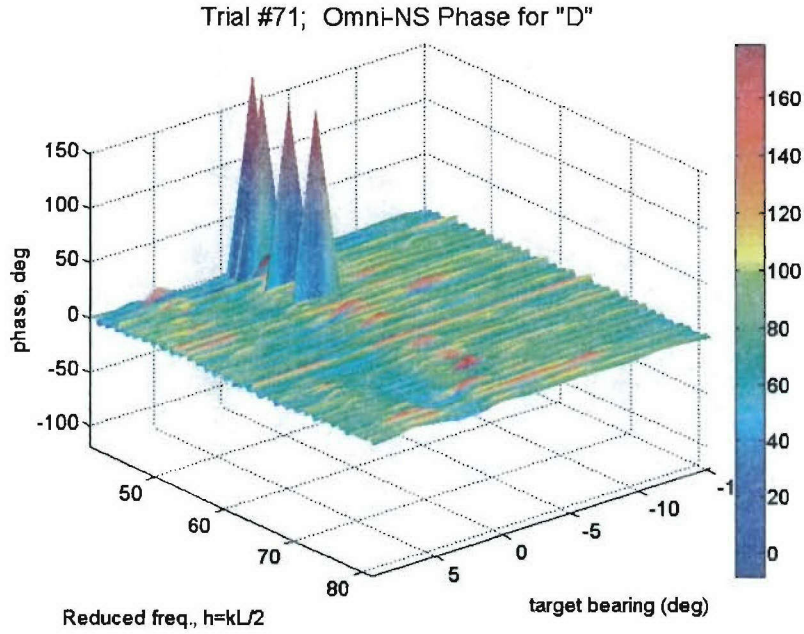


Figure 32. Cross-spectral phase spectra measured between the omni-channel and the N-S directional channel for sensor *D* as the source sweeps out the forward-scattering angles indicated on one of the abscissas. The sensor is along the  $0^\circ$  bearing.

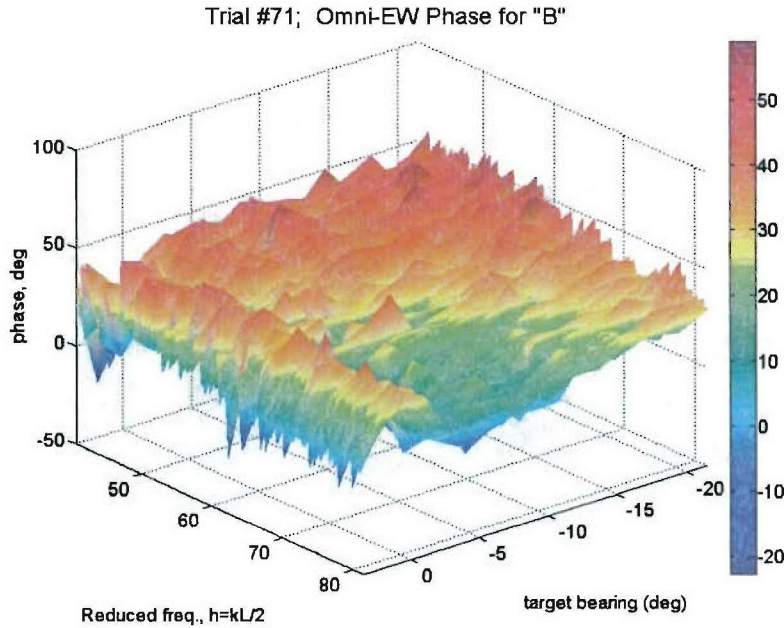


Figure 33. Cross-spectral phase spectra measured between the omni-channel and the E-W directional channel for sensor *B* as the source sweeps out the forward-scattering angles indicated on one of the abscissas. The sensor is along the  $0^\circ$  bearing.



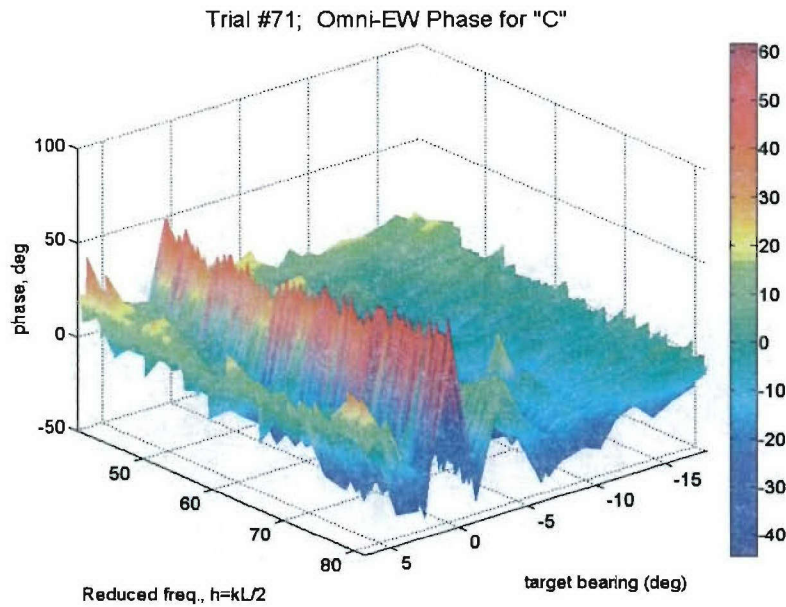


Figure 34. Cross-spectral phase spectra measured between the omni-channel and the E-W directional channel for sensor C as the source sweeps out the forward-scattering angles indicated on one of the abscissas. The sensor is along the  $0^\circ$  bearing. Note side-lobes at  $\pm 4.5^\circ$  as predicted by theory.

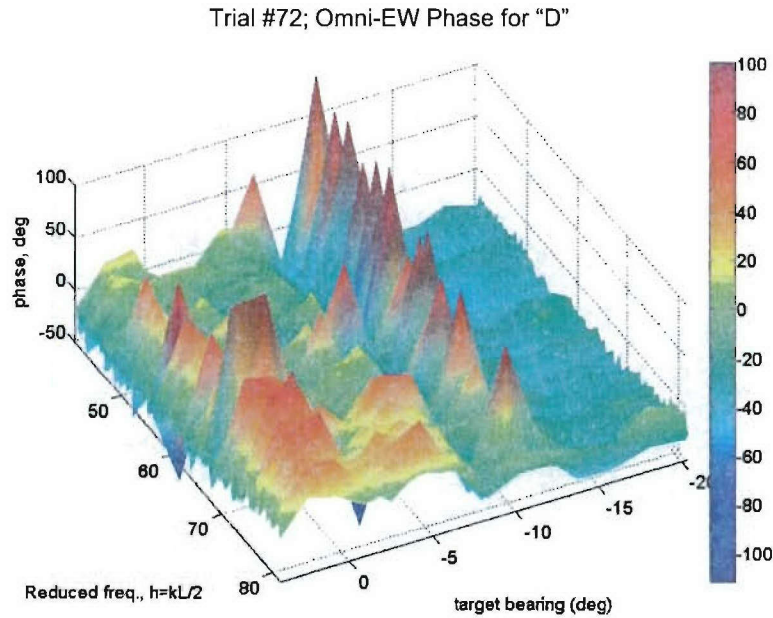


Figure 35. Cross-spectral phase spectra measured between the omni-channel and the E-W directional channel for sensor *D* as the source sweeps out the forward-scattering angles indicated on one of the abscissas. The sensor is along the  $0^\circ$  bearing. Note side-lobe presence at  $-4.5^\circ$ . The phase shifts at about  $-11^\circ$  are due to contaminating source (motorized wench engine).

### 3. *Histogram Representation*

The present data have been presented in the spectral domain because the source was operated continuously with random white noise input, and it is a straight-forward procedure to obtain spectra from a digital signal analyzer. Finite Fourier transforms are computed for each of the time records collected from this continuous signal. In these results there is no overlap of data records. The auto- or cross-spectra are computed according to Eq. (10).

It is also possible to choose a particular frequency bin of the phase spectrum (or any other intensity metric), and perform an amplitude domain statistical analysis on the ensemble of measured phase values. One output of this type of procedure is the histogram. Histograms of the data presented in Figs. 34 and 35 are given in Figs. 36 and 37 for the frequencies of 1500 ( $h = 61.1$ ) and 1875 Hz ( $h = 76.4$ ), respectively. The histogram representations show in quite dramatic terms the presence of the object in the forward-scattered occlusion zone. The difference in mean phase angle is substantial (between  $40^\circ$  and  $60^\circ$ ).

### Histogram Comparisons – receiver C

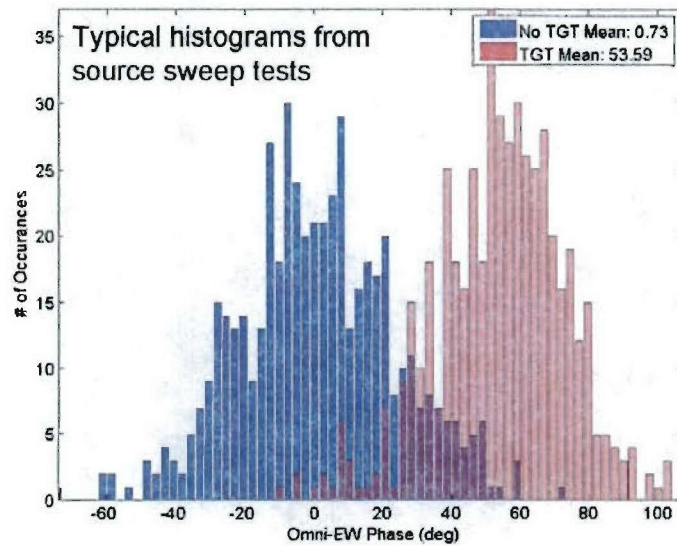


Figure 36. Typical histograms from the source sweep test – sensor *C* at  $h = 61.1$ . The histogram on the left (blue) is for the target well removed from the line-of-sight, while the histogram on the right (red) is obtained for the target on the line-of-sight.

### Histogram Comparisons – receiver D

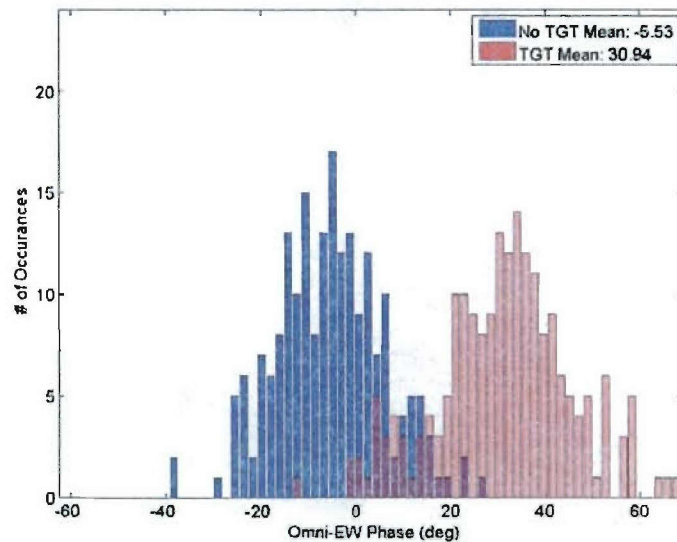


Figure 37. Typical histograms from the source sweep test – sensor *D* at  $h = 76.4$ . The histogram on the left (blue) is for the target well removed from the line-of-sight, while the histogram on the right (red) is obtained for the target on the line-of-sight.



## IV CONCLUSIONS

The use of Directional Frequency Analysis and Recording (DIFAR) acoustic subsystems as underwater acoustic intensity sensors has been demonstrated. Acoustic intensity processing of DIFAR signals has been used to enhance the detection of submerged bodies in the forward-scattered occlusion zone; a zone where the received scalar pressure signal is dominated by the incident blast from the source. According to previously developed theory, the occlusion zone is rich in acoustic pressure gradients. Reactive intensity, and the sine of the phase angle (or the phase angle itself for small angles) between acoustic pressure and particle velocity is proportional to pressure gradient. The experiments, performed at two separate deep water lakes using different targets, were designed to measure intensity phase using standard DIFAR sonobuoys. The receivers were located from 5 to 30 body lengths away from the scattering body, and the source was driven by continuous broadband random noise. All of the effects of lake reverberation are included in the findings. The scalar pressure signal changed insignificantly when the target entered the line-of-sight between the source and receiver because the incident wave arrives simultaneously with the scattered wave and dominates the signal. The cross-spectral phase measured between the pressure and the velocity component in the direction of the incident wave revealed some perturbation due to the presence of the target, but not enough to make it a reliable detection statistic. However, the cross-spectral phase between the pressure and the component of acoustic particle velocity that is orthogonal to the direction of incident wave propagation is a repeatable and strong indicator of the presence of the target in the forward-scattered direction. The measured results support the theory that pressure gradients in the occlusion zone cause measurable perturbations in the intensity phase. The transverse component of intensity phase is a viable indicator of a scattering object in the occlusion zone.

## REFERENCES

1. B. Gillespie, K. Rolt, G. Edelson, R. Shaffer, and P. Hursky, "Littoral target forward scattering," *Acoustical Imaging* **23**, Plenum Press, New York, 501-506 (1997).
2. H. M. Nussenzveig, *Diffraction Effects in Semiclassical Scattering* (Cambridge Univ. Press, Cambridge, Great Britain, 1992).
3. P. Ratilal and N.C. Makris, "Extinction theorem for object scattering in a stratified medium," *J. Acoust. Soc. Am.* **110**, 2924-2945 (2001).
4. G. C. Lauchle, "Short-wavelength acoustic diffraction by prolate spheroids," *J. Acoust. Soc. Am.* **58**, 568-575 (1975).
5. G. S. Sammelmann, D. H. Trivett, and R. H. Hackman, "High-frequency scattering from rigid prolate spheroids," *J. Acoust. Soc. Am.* **83**, 46-54 (1988).
6. A. Sarkissian, C. F. Guammond, and L. R. Dragonette, "T-matrix implementation of forward scattering from rigid structures," *J. Acoust. Soc. Am.* **94**, 3448-3453 (1993).
7. H. Song, W.A. Kuperman, W.S. Hodgkiss, T. Akal, and P. Guerrini, "Demonstration of a high-frequency acoustic barrier with a time-reversal mirror," *IEEE J. Ocean. Eng.* **28**, 246-249 (2003).

8. N. Willis, *Bistatic Radar* (Artech House, Boston, MA, 1991).
9. A. D. Pierce, *Acoustics: An Introduction to its Physical Principles and Applications* (Acoustical Society of America, New York, p. 430, 1989).
10. B. R. Rapids and G. C. Lauchle, "Processing of forward scattered fields with intensity sensors," *Proc. Oceans 2002*, Biloxi, MS, October 29-31, 2002, pp. 1911-1914.
11. B. R. Rapids and G. C. Lauchle, "Acoustic intensity measurements involving forward scatter from prolate spheroids," *J. Acoust. Soc. Am.* **116**, 2528 (2004).
12. B. R. Rapids, "Acoustic Intensity Methods in Classical Scattering," Ph.D. Thesis in Acoustics, The Pennsylvania State University (2004).
13. B. R. Rapids and G. C. Lauchle, "Vector intensity field scattered by a rigid prolate spheroid," accepted for publication in *J. Acoust. Soc. Am.* (July 2005).
14. G. L. D'Spain, "Energetics of the ocean's infrasonic sound field," Ph.D. Thesis in Oceanography, University of California, San Diego (1990).
15. H. R. Race, "Development of a digital DIFAR demultiplexer and bearing tracker module," M.S. thesis, Naval Post-Graduate School, 1999.